scientific data

OPEN

DATA DESCRIPTOR

An aerial color image anomaly dataset for search missions in complex forested terrain

Rakesh John Amala Arokia Nathan[1,3], Matthias Gessner[2,3], Nurullah Özkan[1,3], Marius Bock[2], Mohamed Youssef[1], Maximilian Mews[2], Björn Piltz[2], Ralf Berger[2] & Oliver Bimber[1,3] ✉

After a family murder in rural Germany, authorities failed to locate the suspect in a vast forest despite a massive search. To aid the search, a research aircraft captured high-resolution aerial imagery. Due to dense vegetation obscuring small clues, automated analysis was ineffective, prompting a crowd-sourcing initiative. This effort produced a unique dataset of labeled, hard-to-detect anomalies under occluded, real-world conditions. It can serve as a benchmark for improving anomaly detection approaches in complex forest environments, supporting manhunts and rescue operations. Initial benchmark tests showed existing methods performed poorly, highlighting the need for context-aware approaches. The dataset is openly accessible for offline processing. An additional interactive web interface supports online viewing and dynamic growth by allowing users to annotate and submit new findings.

Background & Summary

On 6 April 2025, a family was brutally murdered in their home in the middle of the night in Weitefeld, a small German village. The prime suspect was believed to have fled into the nearby forest, a sprawling 60-square-kilometer area. Despite an extensive search involving over a thousand police officers, helicopters, drones, and divers, the perpetrator remained at large. The sheer size of the search area, combined with dense vegetation, made the operation extremely challenging. After three weeks with no breakthroughs, authorities concluded that the suspect was most likely dead. Yet, locating his remains was crucial—not only to bring closure to the case but also to ease the lingering fear among residents of Weitefeld and neighboring villages, who were left in the unsettling limbo of a cold case. To advance the search, Johannes Kepler University, the German Aerospace Center, and the Rhineland-Palatinate police. On 27 April 2025, a research aircraft took off from Würselen Airfield in Aachen, Germany, equipped with a specialized modular aerial camera system. Its mission was to scan a 25-square-kilometer section within the search area, capturing high-resolution (8,416 × 6,032 pixels) aerial imagery to detect anomalies, such as clothing or shelters that might indicate human remains. During the flight, the plane captured 30,454 RGB images with a ground resolution of approximately 4 × 4 centimeters per pixel. However, due to dense vegetation obscuring potential clues —some of which might span just a few pixels— automated object classification was unrealistic. Instead, an online crowd-sourcing initiative, enlisting 160 volunteers, was applied to a 10-square-kilometer priority zone of the scan section to manually analyze a subset of 10,659 images for irregularities. This crowd sourcing was supported by automatic color anomaly detection[1]. A total of 405 anomalies were found and categorized as potential objects, shelters, persons, or unknown. 238 of these findings were considered relevant for the case and were subsequently verified by ground police teams (cf. Fig. 1). Despite these efforts, the mission ultimately did not locate the suspect, leaving the case unresolved. Nevertheless, the operation yielded a valuable dataset of 34,424 labeled and categorized anomalies across 405 findings appearing from different viewing angles and at different occlusion conditions in 10,659 aerial images (Fig. 2 illustrates examples). Each of the findings was identified during ground observations by police, and the corresponding protocols are provided. Furthermore, we supply additional 19,795 unlabeled aerial images covering two non-priority zones (regions west and east of the priority zone) of the scan section, which facilitate future labeling and data acquisition. The dataset and the web interfaces used for the crowd sourcing is available online,

[1]Johannes Kepler University, Institute of Computer Graphics, Linz, 4040, Austria. [2]German Aerospace Center, Institute of Space Research, Berlin, 12489, Germany. [3]These authors contributed equally: Rakesh John Amala Arokia Nathan, Matthias Gessner, Nurullah Özkan, Oliver Bimber. ✉e-mail: oliver.bimber@jku.at

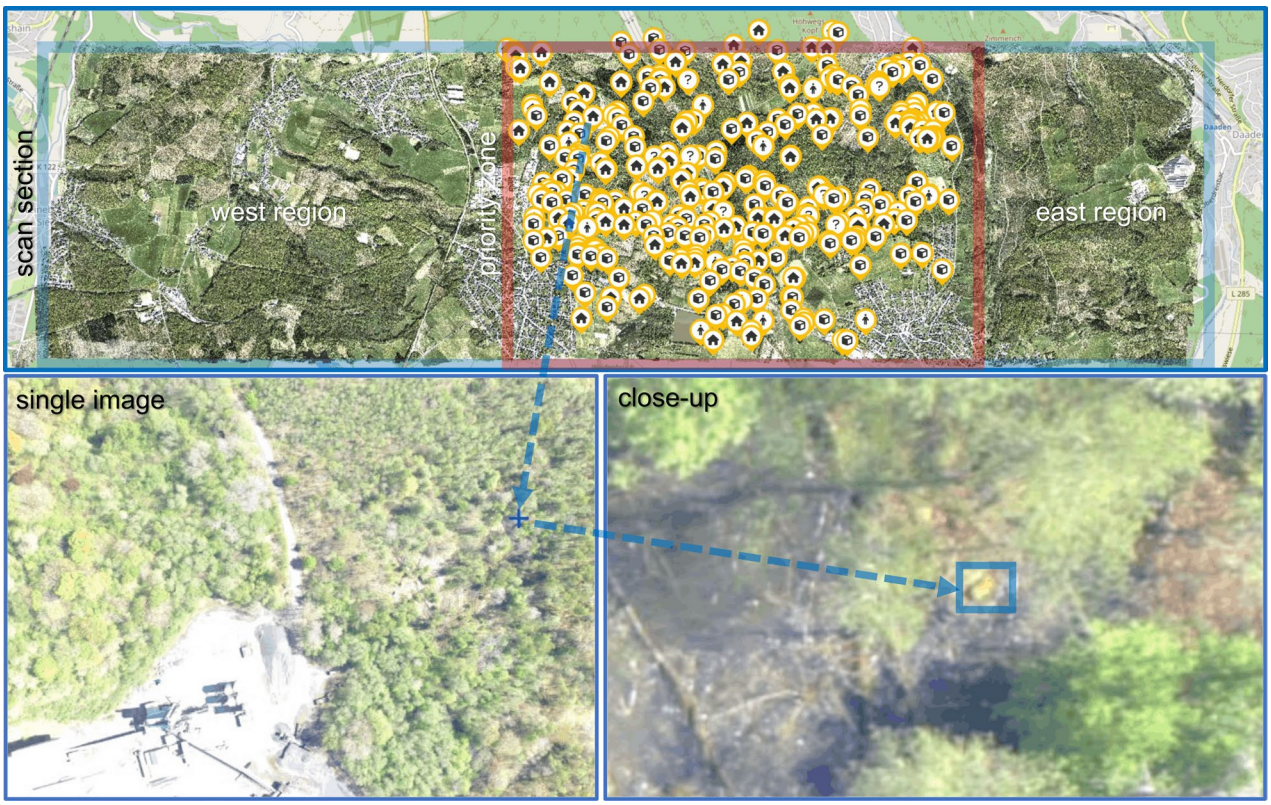

Fig. 1 Map of scan section and priority zone with orthographically projected aerial images of the flight and locations of relevant findings (top). Example finding in full aerial image and close-up (bottom). During ground observation, this finding was later identified as "a small barrel, very old, partially overgrown and filled with soil".

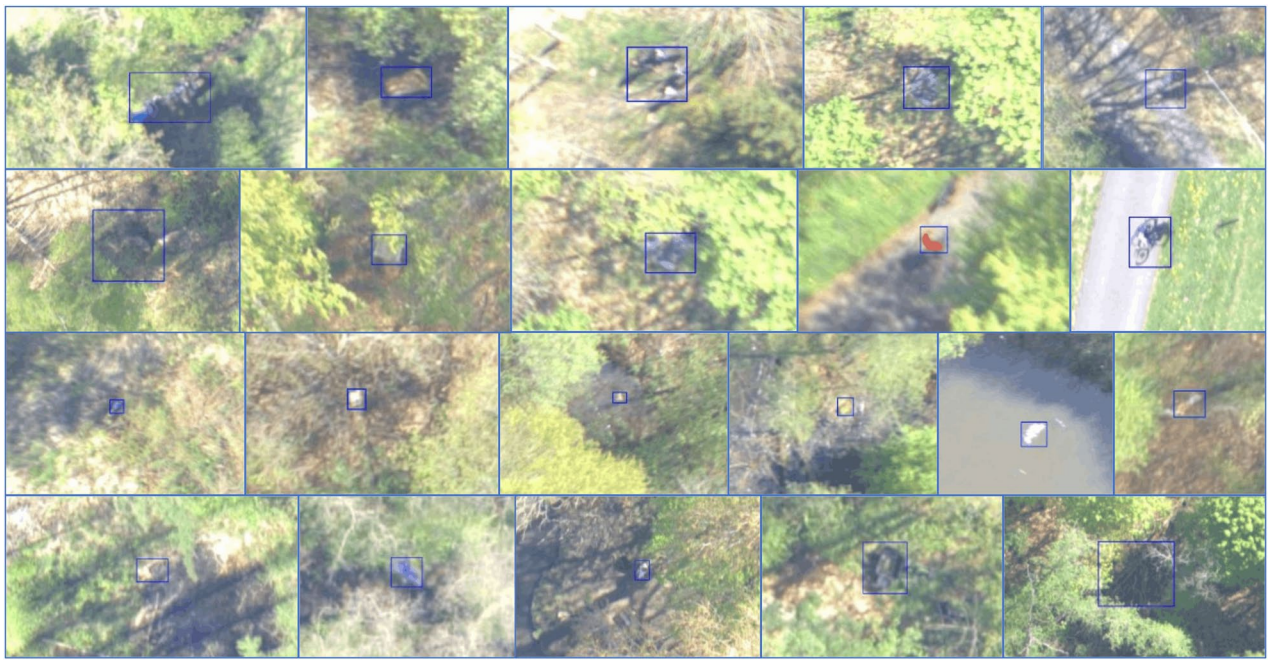

Fig. 2 Close-ups of various sample findings contained in the dataset together with their bounding-box labels. Overall, they include objects such as barrels, trash bags, tarps, metal barriers, floating objects on water; but also people and potential man-made shelters, hunting stands, sheds, huts, tents, shooting ranges, fire pits, and others – all identified based on color and structural anomalies.

Dataset	Year	Image Type	Size (Train/Val/Test)	Resolution	Application
MVTec AD[58,59]	2019	RGB, Grayscale	5,354	700 × 700 1,024 × 1,024	Industrial Inspection
MVTec AD 2[60]	2025	RGB, Grayscale	8,004 (2,528/302/5,174)	2,232 × 1,024 2,448 × 2,048 2,100 × 1,520 4,224 × 1,056 1,400 × 1,900	Industrial Inspection
MVTec LOCO AD[30]	2022	RGB	3,644 (1,772/304/1,568)	1,600 × 1,280 1,600 × 1,100 1,700 × 1,000 1,700 × 850 800 × 1,600	Industrial Inspection
MVTec 3D-AD[61]	2021	RGB	4,147 (2,656/294/1,197)	800 × 800 400 × 400 500 × 500 900 × 900 600 × 600 900 × 400 600 × 800	Industrial Inspection
beanTech Anomaly Detection (BTAD)[62]	2021	RGB	2,830	1,600 × 1,600 600 × 600 800 × 600	Industrial Inspection
Thermal Anomaly Detection[36,70]	2022	Thermal	39,600	288 × 384	Visual Surveillance
UCSD Ped1[63]	2010	Grayscale	14,000	238 × 158	Visual Surveillance
UCSD Ped2[63]	2010	Grayscale	4,560	360 × 240	Visual Surveillance
Fishyscapes Lost and Found[73,74]	2019	RGB	375	2,048 × 1,024	Autonomous Driving
Visual Anomaly Dataset (VisA)[75]	2022	Grayscale	10,821	4,000 × 6,000	Industrial Inspection
RoadAnomaly21[71]	2021	RGB	110	2,048 × 1,024 1,280 × 720	Autonomous Driving
RoadObstacle21[71]	2021	RGB	357	1,920 × 1,080	Autonomous Driving
Manipal UAV Anomalous Activity Dataset (MUAAD)[68]	2022	RGB	68,687	1,280 × 720	UAV-based Surveillance
Drone-Anomaly[67]	2022	RGB	87,488	640 × 640	UAV-based Surveillance
CUHK Avenue[64]	2013	RGB	30,652	640 × 360	Visual Surveillance
ShanghaiTech[66]	2017	RGB	3,17,398	856 × 480	Visual Surveillance
UIT-ADrone[69]	2023	RGB	2,06,194	1,920 × 1,080	UAV-based Surveillance
Highway Traffic Anomaly (HTA)[72]	2020	RGB	~ 400,000	1,280 × 720	Visual Surveillance
ADOC[65]	2020	RGB	2,59,127	2,048 × 1,536	Visual Surveillance
Street Scene[76]	2020	RGB	2,03,257	1,280 × 720	Visual Surveillance
San Diego airport[78]	2002	Hyperspectral	1	400 × 400 × 224	Remote Sensing
Viareggio[81]	2013	Hyperspectral	1	450 × 375 × 511	Remote Sensing
HYDICE Forest[79]	1995	Hyperspectral	1	64 × 64 × 210	Remote Sensing
HYDICE Urban[77]	1995	Hyperspectral	1	307 × 307 × 210	Remote Sensing
MUUFL Gulfport (MUUFL)[80]	2010	Hyperspectral	1	325 × 220 × 64	Remote Sensing
Weitefeld (ours)	**2025**	**RGB**	**10,659 (labeled), 19,795 (unlabeled), extendable**	**8, 416 × 6, 032**	**Complex Forested Terrain (e.g., SAR, manhunt)**

Table 1. Overview of Image Anomaly Detection Datasets.

enabling to view, analyze, and additionally label these images and findings. For validation, we applied our dataset to benchmark several common color anomaly detection methods, including deep-learning-based approaches (Feature Reconstruction Error (FRE)[2], FastFlow[3], Efficient AD[4]) and model-based techniques (Reed-Xiaoli Global (RXG)[1], Reed-Xiaoli Modified (RXM)[5], principal component analysis (PCA)[6]). We found that all of them performed poorly on our data – especially in case of strong occlusion caused by vegetation. A key reason for this failure is that decisions based on local image regions or individual pixels lack the broader contextual information that our human volunteers utilized. For instance, occurring structures such as tree stumps, that are conspicuous in isolation may not be flagged as anomalies when appearing frequently across a wider area. We believe that our real-world, large-scale search effort under challenging and realistic conditions provides a unique resource for improving and benchmarking automatic image anomaly detection algorithms which are critical for search-and-rescue missions and manhunts in complex, forested terrain. Such a dataset did not exist before.

On August 5, 2025, the severely decomposed body of the murderer was discovered in an open field near Weitefeld, approximately 200 meters from where our flight plan had ended. It emerged that he had taken shelter inside an underground concrete water pipe about 100 meters away, where he died. His weapon was also found inside the pipe. Months later, a heavy rainfall event washed the body out to the location where it was ultimately discovered.

Related Works & Datasets. Anomaly detection in visual data plays a vital role in numerous real-world applications where rapid and accurate identification of irregularities is essential. Key domains include search and rescue (SAR) operations[7–16] where identifying visual anomalies can help to locate individuals or objects of interest in vast and complex terrains, wildlife monitoring[17] where deviations in species behavior or distribution can signal ecological threats, and automated industrial inspection[18–26] where the detection of defects ensures quality control and operational safety. The nature of the task often depends on the imaging modality, leading to distinct categories such as color-based anomaly detection[8–10,15,16,27,28], structural anomalies (e.g., geometric deformations or missing components in manufactured parts[29,30]), thermal irregularities[31–38], and spectral anomalies involving multispectral or hyperspectral imagery[5,39–48]. Advances in deep learning[49–53] and model-based frameworks[1,54–57] have significantly improved the robustness, generalization, and real-time applicability of anomaly detection systems.

A variety of publicly available datasets support the development and benchmarking of anomaly detection techniques across multiple domains (see Table 1). In industrial inspection, datasets such as the MVTec anomaly detection dataset (MVTec AD)[58,59] and its successors (MVTec AD 2)[60], MVTec logical constraints anomaly detection dataset (MVTec LOCO AD)[30], MVTec 3D anomaly detection dataset (MVTec 3D-AD)[61]) offer RGB and grayscale images of manufactured parts with various types. These datasets span resolutions from 400 × 400 to over 4,000 × 2,000 pixels and include thousands of samples, enabling evaluation of both 2D and 3D anomaly detection. The beanTech anomaly detection BTAD dataset[62] provides additional variety of high-resolution RGB images of manufactured parts for anomaly detection. In the domain of visual surveillance, benchmark datasets such as UCSD Ped1[63] and Ped2[63], CUHK Avenue[64], ADOC[65], and ShanghaiTech[66] focus on anomalous motion patterns and abnormal events. These include non-pedestrian entities appearing in pedestrian walkways and unusual behaviors such as throwing objects. The datasets offer footage in either grayscale or RGB format, typically at moderate resolutions.

UAV-based anomaly detection is supported by datasets such as Drone-Anomaly[67], MUAAD[68], and UIT-ADrone[69], which collectively contain hundreds of thousands of RGB video frames. These datasets primarily focus on general aerial surveillance, capturing anomalous events or patterns in urban or open environments with relatively clear visibility. However, these datasets do not capture the visual complexity of forested environments, including frequent occlusions and clutter, nor are they tailored to the operational requirements of SAR and manhunt scenarios. In the thermal domain, the Thermal Anomaly Detection dataset[36,70] offers nearly 40,000 infrared frames, aiding anomaly detection in low-light or thermally variable settings. For autonomous driving, datasets like RoadAnomaly21[71], RoadObstacle21[71], Highway Traffic Anomaly (HTA)[72] and Fishyscapes Lost and Found[73,74] provide RGB street-level imagery to identify hazardous or anomalous objects on roads. Additional benchmarks, such as VisA[75], support large-scale industrial inspection with high-resolution RGB imagery spanning 12 objects across 3 domains, while the Street Scene[76] dataset captures real-world urban anomalies. In addition, several datasets using hyperspectral imagery (e.g., environmental monitoring, urban analysis, vegetation and forest assessment)[77–81] enable applications such as spectral anomaly detection. Although these datasets collectively cover a broad spectrum of sensing modalities, resolutions, and application areas, none are designed to support anomaly detection in the highly challenging conditions of densely forested search environments.

Our dataset (Weitefeld) is the first to address search missions in complex forested terrain, such as those encountered in search-and-rescue (SAR) and manhunt operations. It is both large-scale (with tens of thousands of images and labels) and realistic, having been derived from an actual manhunt. While extensive prior work—including datasets and studies such as[82–93], as well as datasets produced by programs such as the IARPA Biometric Recognition and Identification at Altitude and Range (BRIAR) initiative[94], supports person identification and classification for these applications, such methods fail entirely under heavy occlusion caused by vegetation. In these scenarios, classifiers cannot detect or identify objects represented by only a few, sparsely visible pixels. Further degradation from motion blur (e.g., due to high flight speeds and low exposure) and other real-world imaging artifacts exacerbates these limitations. In contrast, anomaly detection remains robust under such conditions, as it does not rely on explicit target appearance, such as that required in the BRIAR dataset[94]. However, it still relies on human intervention to classify detected objects.

Methods

The following subsection summarizes the initial data acquisition and processing steps, the online crowd sourcing, and the subsequent data review, mapping, and ground operations that contributed to our final dataset. The Ethics Committee of Johannes Kepler University approved the data collection and study (application number: JKU EC-55-2025). Informed consent for participation and data sharing was obtained directly from participants.

Data Acquisition and Processing. A specialized aerial camera system (MACS) developed by DLR[95] was installed in an underwing pod of a Stemme S10 motorized glider for image acquisition (cf. Fig. 3). The system combines a visible-light (RGB) camera and a thermal infrared module.

The RGB camera employs a 51-megapixel global shutter CMOS sensor with a Bayer color filter array, 4.60 μm pixel pitch, and 12-bit radiometric resolution, coupled with a fast 50 mm f/2.5 lens. The thermal module uses an industrial microbolometer with a resolution of 1 megapixel, 17 μm pixel pitch, and a 30 mm f/1.0 lens.

Images were captured and processed at a constant frame rate of 10 frames per second, ensuring high overlap and sufficient observation geometries for each ground point, corresponding to a sustained data rate exceeding 6 gigabits per second (Gbps). Higher frame rates, while technically feasible, do not offer any practical advantages in this scenario. Integrated dual-frequency GNSS (Global Navigation Satellite System) and an industrial-grade IMU (Inertial Measurement Unit) enable direct georeferencing, with all images stored as raw 16-bit data.

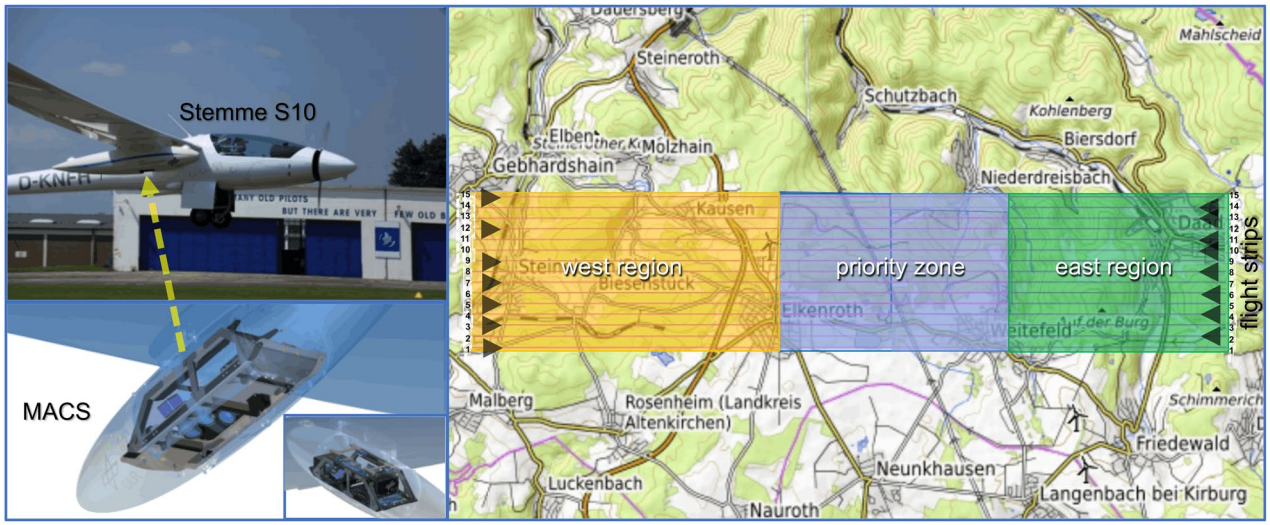

Fig. 3 The research aircraft (a Stemme S10 motorglider, top-left) was equipped with the Modular Aerial Camera System (MACS, bottom-left) mounted in one of its underwing pods. This system was used for data acquisition. The flight plan (right) displays the locations and numbering of the 15 flight strips. GPS coordinates for Weitefeld: 50.72468°N (latitude), 7.92714°E (longitude).

A flight plan was created considering the prioritized zone of interest by the police (3.5 × 2.0 km). In an altitude of 1000 ft (ca. 300 m) above the highest point and with 20% overlap across the flight direction the entire area could be mapped with 15 flight lines. The flight strips ran from south to north with an alternating east/west heading (arrows in Fig. 3), except for two repeated strips, and were extended to both sides to cover also a part of the low priority regions in one flight. Due to the hilly terrain in the area flown over, the resulting ground sampling distance (GSD) is between 3 and 5 cm/pixel. The flight was carried out on 27 April 2025, and to minimize shadows of occluders in the forest area, it was scheduled around the maximum solar altitude (11:26 UTC). The clear weather conditions during the image flight lead to a high radiometric scene contrast in the captured imagery. In order to focus on the dynamic range in shaded areas, assuming that the person is more likely to be there, the exposure time was set to a rather high 1.3 ms. The resulting motion blur (ground smear) and a certain overexposure in bright areas was tolerated.

After the flight the raw images were post-processed as follows:

- Removing images that mainly shown urban areas.
- Correction of dark signal non-uniformity, photo response non-uniformity and a color adjustment using parameters from a radiometric calibration.
- Reconstruction of full-color RGB images from the raw Bayer-pattern sensor data using the DCB demosaicing algorithm[96].
- Gamma correction with 0.37 (adjusting tonal range by applying a power-law transformation to pixel intensity values).
- Color saturation was scaled by factor 2 to compensate for image degradation due to the high exposure times.
- Images were reduced to 24-bit color depth (8 bit per color channel) and JPEG-compressed at a rate of 60% (13 MB typically, while keeping the full geometric resolution of 8,416 × 6,032 pixels) to ensure efficient online crowd sourcing even with limited network bandwidth.

To guide the online crowd sourcing in such high-resolution images, we generated a binary anomaly mask for each image using the Reed-Xiaoli (RX) color anomaly detector[1], with an anomaly threshold set to 0.985. The binary mask was then multiplied with the corresponding RGB image to produce a color anomaly mask. The colors in these masks correspond to the original RGB content. Any remaining visible colors represent the original pixels. All processing was performed in parallel on 8 high-end PCs and completed in approximately 30 minutes. The resulting 10,659 image pairs (RGB + color anomaly mask) were then used for the online crowd sourcing.

Online Crowd Sourcing. For the online crowd sourcing, an html-based and a JavaScript-based frontend (using OpenSeadragon and JSZip) has been developed (cf. Fig. 4). It supports browsing through the images recorded within the same flight strip using keyboard shortcuts (A/D), or switching to a different flight strip by entering the unique image identifier (lower left corner). Users can switch between RGB images and anomaly masks using keyboard shortcuts (W/S), zooming using the mouse wheel and panning using the arrow keys or left mouse button, brightness (gamma) changes can be done using the keyboard shortcuts (+/−), point (marker) labeling can be performed using Ctrl + click and bounding box labeling can be done using Alt + drag to mark and classify regions of findings. Marked points or bounding boxes can be assigned classes and comments via

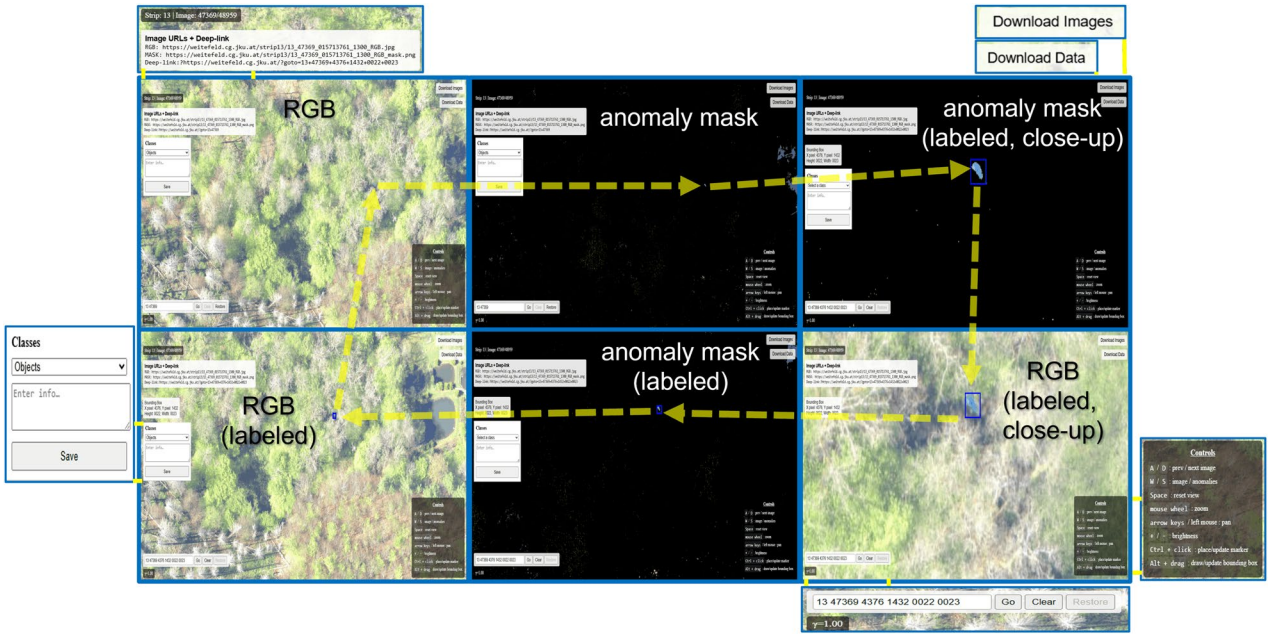

Fig. 4 Image analyzer web-frontend used for online crowd sourcing and subsequent reviews of findings. It supports browsing image sequences from the same flight strip, toggling between RGB images and anomaly masks, zooming into specific areas, panning across details, adjusting brightness, and performing point- or bounding-box labeling, as well as classifying findings and adding comments.

the context menu that appears after marking a finding. Users can also download images and retrieve URLs and deep-links for both RGB images and anomaly masks using the Download Images and Download Data buttons, located in the top-right corner of the interface. Keyboard shortcuts and available actions are summarized in the controls panel shown in the bottom-right corner of the interface, allowing users to efficiently navigate, annotate, and classify images while maintaining consistency during the annotation process.

By entering a unique identifier (lower left corner), volunteers were forwarded to the first image of their assigned batch. This identifier has the following encoding: *AA BBBBB*, where *AA* is the flight strip number and *BBBBB* is the image number. After labeling a finding, this identifier is extended as follows: *AA BBBBB CCCC DDDD* if the label is a marker (point), where *CCCC DDDD* are the x,y pixel coordinates of the label. *AA BBBBB CCCC DDDD EEEE FFFF* if the label is a bounding box, where *CCCC DDDD* are the x,y pixel coordinates of the lower left corner, and *EEEE FFFF* are the height and width.

Each volunteer was assigned overlapping batches of 110 consecutive images and instructed to examine them for anomalies that might suggest the presence of a hidden or deceased person. This included identifying conspicuous objects that seemed out of place in a forest environment, as well as potential shelters or hiding spots. To aid in their assessment, we advised volunteers to toggle between RGB images and anomaly masks, zoom in on specific areas, pan across details, and adjust brightness as needed for better visibility. Since the images in each batch were captured sequentially during flight, the gradual shift in perspective could help reveal gaps in vegetation that a single viewpoint might obscure. Participants were reminded that the precomputed anomaly masks serve only as a supplementary aid and should not be solely relied upon, as they could produce false positives or overlook relevant areas. Regions depicting villages could be disregarded. Any findings were to be marked on just one image, even if they appeared in multiple frames, and volunteers were encouraged to provide a brief subjective classification alongside each label.

The online crowd sourcing took place from 2:00 PM on April 29th, 2025, until 8:00 AM on May 4th, 2025. During this period, a total of 405 findings were reported by 160 volunteers (members of the Rhineland-Palatinate police, students and staff of Johannes Kepler University and the German Aerospace Center, as well as students of the Berlin University of Technology).

Data Review, Mapping, and Ground Operations. Following the online crowd sourcing, all findings were reviewed using the web-based frontend (cf. Fig. 4). Bounding box labels were added to cases initially marked only with point labels. Of the 405 findings, 238 were flagged as relevant, while the remaining 16 –though containing anomalies– were deemed irrelevant to the mission (e.g., cyclists on bike paths, etc.). All findings (categorized, prioritized, and annotated with comments) were then compiled into an interactive online map (cf. Fig. 1). Findings are represented on the map as clickable pins. Selecting a pin reveals a panel displaying key information: the finding's ID, category, volunteer-submitted comments, results from ground checks, and links to Google Maps and the Image Analyzer. Additionally, a map filter enables users to show only findings of specific categories. This map assisted police ground operations by providing precise GPS navigation to target locations via mobile devices.

The ground operation was conducted on May 5th and 7th, 2025, during which police forces inspected all 238 relevant findings. The large-scale operation also required clearing wooded areas to access overgrown zones, as well as deploying divers and sonar scans to examine small lakes and ponds. The police reports documenting the on-site findings are included in our dataset.

While the initial crowd sourcing effort labeled the 405 anomalies only in individual images, photogrammetry was used to project these labels onto every image depicting the same finding (under different perspectives and occlusion conditions). Techniques applied included bundle block adjustment, triangulation, and collinearity-based back-projection. The imaging frame rate (10 Hz) caused overlap in strip direction (up to 85 times), ultimately generating 34,424 distinct anomaly labels across 10,659 perspective images within the priority zone.

Data Records

Our dataset is accessible through multiple sources:

- The core dataset obtained from our crowd sourcing, used for benchmarking, is available for bulk download at: https://zenodo.org/records/15848419[97] (approx. 144.1GB). This is the static, peer-reviewed version of the annotated dataset; any new annotations added after peer review will be made available via the interactive platform (https://weitefeld.cg.jku.at/). It contains 34,424 labeled and categorized anomalies across 405 findings, captured under different viewing angles and occlusion conditions in 10,659 aerial images taken within the priority zone.
- The core dataset and the additional 19,795 unlabeled aerial images covering the two non-priority zones are available for bulk download and online viewing at https://weitefeld.cg.jku.at/(approximately 404 GB). The interactive web-interface (cf. Fig. 4) also supports adding new labels to extend the core dataset in the future.
- A map overview of the entire dataset is available at https://macs.dlr.de/weitefeld/(cf. Fig. 1).

Downloading the Dataset. *Using the web-interface.* Aerial images can be downloaded via the Download Images button (top-right corner) of the Image Analyzer web-frontend (https://weitefeld.cg.jku.at/). To request a batch of images, users must specify the first and last image in the batch using the format *AA BBBBB*, where *AA* denotes the flight strip number (cf. Fig. 3) and *BBBBB* represents the image number (cf. Table 2). Upon submission, a .zip file containing the requested batch is automatically downloaded. The filenames use the following format: AA_BBBBB_JJJJJJJJJ_KKKK_RGB.jpg. In this naming convention, *AA BBBBB* repeats the strip and image numbers from earlier, *JJJJJJJJJ* represents a second-precise camera-internal time-stamp, while *KKKK* adds microsecond-precision. A typical example would be 8_27015_012318083_1300_RGB.jpg. Note that the full image dataset has a size of 404.44 GB.

The associated findings data can be downloaded by clicking the Download Data button in the top-right corner, which provides the findings database (data.txt). Each entry follows this structured format: *AA BBBBB CCCC DDDD G "HHH...HHH" AA BBBBB CCCC DDDD EEEE FFFF "III...III"*, where *AA* represents the flight strip number, *BBBBB* denotes the image number, *CCCC DDDD* indicates the x,y pixel coordinates of a point (marker) label, *G* specifies the class number (0=unknown, 1=shelter,2=object, 3=person), and *HHH...HHH* contains the volunteer's comment. The second part of the entry includes repeated strip and image numbers (*AA BBBBB*) followed by *CCCC DDDD* representing the x,y coordinates of the lower-left corner of a bounding box label, *EEEE FFFF* specifying the box's height and width, and *III...III* containing the police's ground operations comment. A typical example would be *07 23724 7844 0754 1 "Looks like some sort of shelter or roof of something." 07 23724 7796 0795 0074 0068 "Tarp, tent, self-made, possibly by children, near edge of town, inconspicuous."*. Missing entries are marked as *NA*. For instance, an entry without a police comment appears as *06 19341 0515 5798 0 "A blue thing which does not seem as it was created by nature." 06 19341 0501 5809 0026 0025 NA*. An entry containing only a point label (no bounding box or police comment) would be *07 23343 0285 1701 0 "Looks like a human-like shape with orange clothing, or wrapped in orange/bright plastic." -1 -1 -1 -1 -1 -1 "NA"*. Note, that we use -1 and "NA" to indicate integers and strings that are not available.

Using Zenodo. Aerial images of the priority zone and corresponding findings from the crowd sourcing are downloadable in 15 zip files and one .txt file (https://zenodo.org/records/15848419)[97]. The .zip file names indicate the strip number (e.g., stip7.zip contains aerial images from flight strip 7). The naming convention of the arial images inside each .zip file is as described above. The file data.txt contains the findings database in the exact format specified above. Note that this dataset has a size of 144.1 GB.

Viewing the Dataset Online. The image analyzer web-frontend enables direct viewing of aerial images and associated findings in a web browser. To access specific content, users can copy one of three unique identifier formats into the text box located in the lower-left corner (see Fig. 4). These identifiers, available in the findings database (data.txt), follow these patterns: The basic format *AA BBBBB* displays image number *BBBBB* from flight strip *AA*. For point label visualization, the format extends to *AA BBBBB CCCC DDDD*, where *CCCC DDDD* represents the pixel coordinates within the specified image. The most comprehensive format, *AA BBBBB CCCC DDDD EEEE FFFF*, displays a bounding box with its lower-left corner at *CCCC DDDD* and dimensions of *EEEE* (height) by *FFFF* (width). Example identifiers include *14 57026* for basic image display, *03 09072 4497 0371* for point label viewing, and *13 47790 6828 4800 0017 0016* for bounding box visualization. For detailed instructions on navigating the image analyzer web-frontend, please refer to the *Online Crowd Sourcing* section.

Strip Number	Image Numbers (West Region)	#Images (West Region)	Image Numbers (Priority Zone)	#Images (Priority Zone)	Image Numbers (East Region)	#Images (East Region)	Total
01	01677 → 02588	1,020	02856 → 03240	385	03521 → 03525	446	**1,851**
	02748 → 02855				03545 → 03985		
02	05968 → 05988	738	05527 → 05967	441	04642 → 05311	670	**1,849**
	06153 → 06869						
03	08077 → 08861	785	09067 → 09582	516	09756 → 10387	632	**1,933**
04	12846 → 13493	648	12051 → 12721	671	11326 → 11583	682	**2,001**
					11602 → 12025		
05	15000 → 15715	716	15865 → 16667	803	16668 → 16700	667	**2,186**
					16701 → 17196		
					17262 → 17432		
06	19963 → 20582	620	19131 → 19838	708	18310 → 18614	718	**2,046**
					18693 → 19105		
07	22362 → 23097	736	23133 → 23885	753	23899 → 24385	646	**2,135**
					24477 → 24635		
08	27551 → 28214	664	26698 → 27482	785	25887 → 26129	712	**2,161**
					26229 → 26697		
09	29664 → 30422	759	30509 → 31279	771	31280 → 31757	487	**2,017**
					31886 → 31894		
10	34510 → 34516	703	33778 → 34509	732	33321 → 33777	457	**1,892**
	34545 → 34928						
	34962 → 35273						
11	41176 → 41338	817	40407 → 41175	769	38666 → 38677	506	**2,092**
	41382 → 41611				39913 → 40406		
	41663 → 42086						
12	42973 → 43499	865	44019 → 44854	836	44855 → 45321	467	**2,168**
	43565 → 43727						
	43844 → 44018						
13	48024 → 48205	722	47264 → 48023	760	46811 → 47263	453	**1,935**
	48352 → 48444						
	48513 → 48959						
14	57807 → 57956	718	56961 → 57806	846	56507 → 56960	454	**2,018**
	58165 → 58250						
	58315 → 58796						
15	59901 → 59904	810	60972 → 61854	883	61855 → 62331	477	**2,170**
	59919 → 59920						
	59923 → 59933						
	59936 → 60444						
	60482 → 60588						
	60795 → 60971						
Total		**11,321**		**10,659**		**8,474**	**30,454**

Table 2. Image Numbers per Flight Strip (FIRST IMAGE → LAST IMAGE of contentious image segment).

Adding new Findings. To facilitate future expansion of our dataset, the image analyzer web-frontend supports labeling of new findings. Users can annotate either additional discoveries within already-labeled aerial images of the priority zone, or in previously unlabeled images from the two non-priority zones. The interface allows creation of both point (marker) and bounding box labels. After placing a label, users can classify the finding and add comments using the controls in the top-left corner (cf. Fig. 4). All annotations are subsequently saved to the findings database (data.txt). Additional guidance for using the image analyzer web-frontend is available in the *Online Crowd Sourcing* section. Note, that the core dataset obtained from our crowd sourcing and used for benchmarking, is unchangeable. The core dataset findings occupy the first 34,424 entries in the findings database. All subsequent entries represent later additions appended to the database, enabling continuous expansion of the dataset with new user-contributed labels, which are readily downloadable and could potentially support the development of state-of-the-art algorithms.

Technical Validation

To demonstrate the applicability of our dataset, we conducted a simple benchmarking study to evaluate both deep-learning-based (Feature Reconstruction Error (FRE)[2], FastFlow[3], Efficient AD[4]) and model-based (i.e., non-learning, analytically defined, color-statistics-driven) (Reed-Xiaoli Global (RXG)[1], Reed-Xiaoli Modified (RXM)[5], principal component analysis (PCA)[6]) color anomaly detectors. Each detector produces an anomaly

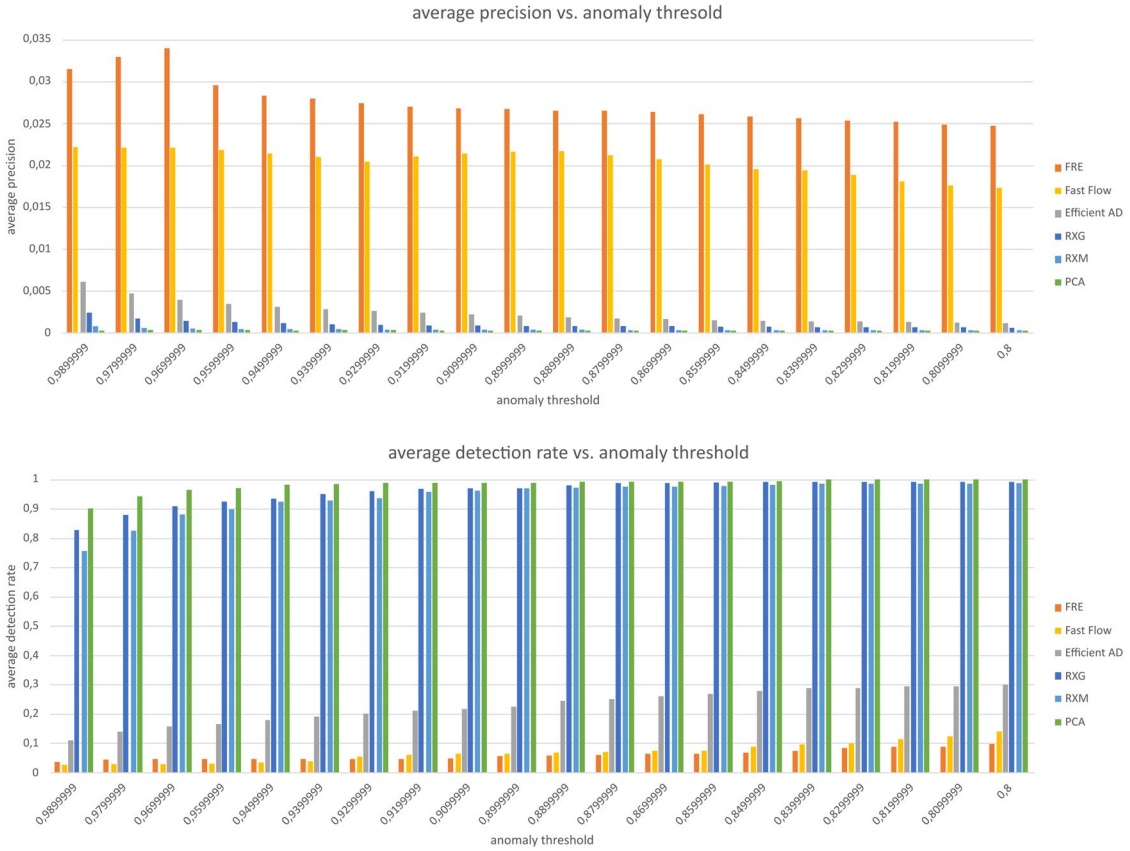

Fig. 5 A comparison of common deep-learning-based (FIRE, FastFlow, EfficientAD) and model-based (RX-G, RX-M, PCA) color anomaly detectors, evaluated in terms of average precision (top) and average detection rate (bottom) across a range of anomaly thresholds t (x-axis).

score for every pixel or region, which is compared against a predefined anomaly threshold ($t \in [0, 1]$) to classify pixels or regions as anomalous. The optimal threshold depends on the specific image content, so to make the evaluation independent of a particular threshold choice, we assess performance across a wide range of threshold values. By sweeping a range of t, we generated binary anomaly masks for each detector and threshold, subsequently comparing these against the annotated findings in our dataset. We assessed performance using two key metrics: *Average precision*, defined as the ratio of true positives (the number of abnormal pixels correctly identified within the bounding boxes) to the sum of true positives and false positives (the total number of pixels flagged as abnormal), averaged across all images. *Average detection rate*, calculated as the proportion of cases where at least one abnormal pixel was detected within the bounding box of a finding, relative to the total number of findings.

For the deep-learning-based detectors, we employed the pre-trained models without fine-tuning. To maintain computational efficiency, we restricted our analysis to the images where findings were originally labeled by volunteers, omitting backprojections. The overall results of this evaluation are summarized in Fig. 5. We also benchmarked the detectors for individual classes (i.e., persons, objects, shelters, and unknown). These results are presented in Figs. 6 and 7. All findings, their associated bounding box annotations and classifications underwent rigorous manual verification before benchmarking to ensure label and class accuracy as far as possible.

Overall, we observe that model-based color anomaly detectors tend to achieve low precision at high detection rates, whereas deep-learning-based approaches exhibit the opposite behavior. The former is caused by a high number of detected anomalous pixels per image (with numerous false positives), while the latter results in sparser detections (with many false negatives). We believe that this discrepancy arises because deep-learning-based models are pre-trained on ImageNet data, which contains significantly different feature representations and statistical distributions compared to our occluded anomalies. In contrast, model-based approaches rely solely on color-space statistics without accounting for higher-level image features at all.

For both types, we observe that as the anomaly threshold increases, precision decreases while the detection rate rises (this holds even when comparing methods within individual classes, as shown in Figs. 6 and 7). A lower anomaly threshold results in more detected anomalies (both true and false). However, since false anomalies tend to occur across entire images –unlike true anomalies, which are confined to relatively small bounding boxes– their number is significantly higher. Consequently, larger objects (e.g., shelters) generally yield higher precision values than smaller ones (see Figs. 6 and 7).

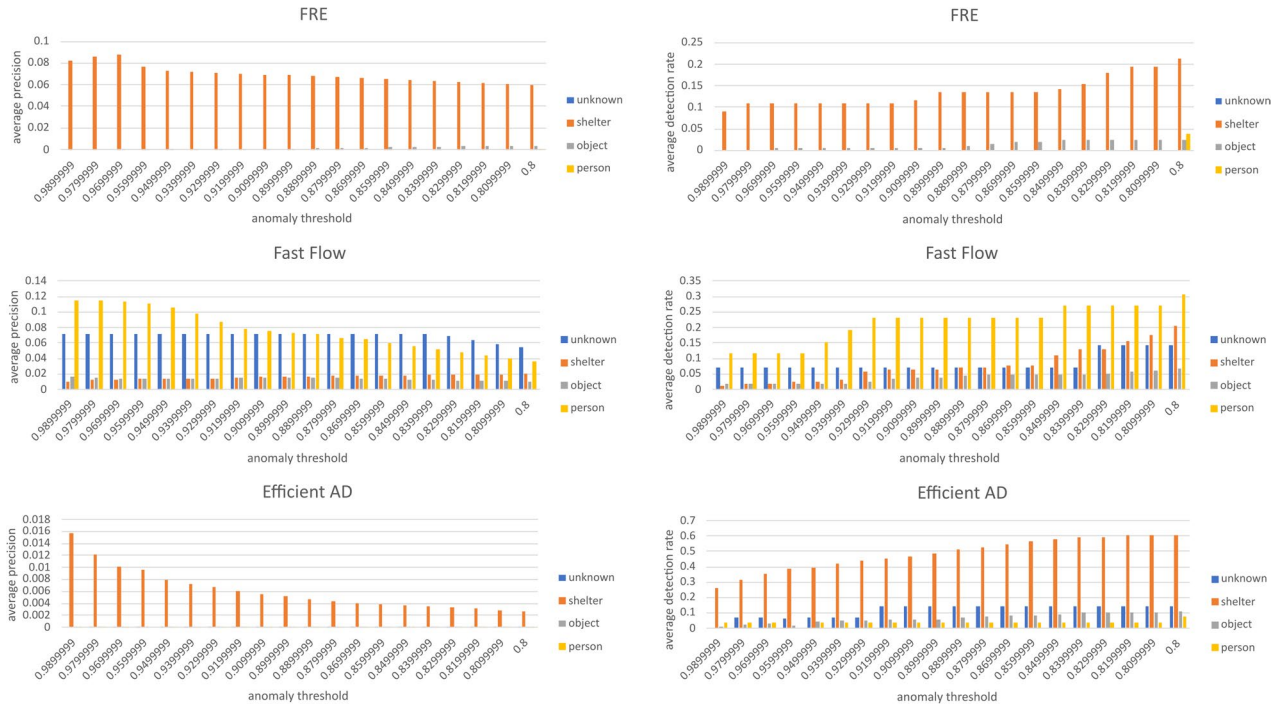

Fig. 6 Performance of deep-learning-based color anomaly detectors (FRE, FastFlow, EfficientAD) over each class (unknown, shelter, object, person). Anomaly threshold vs. average precision (left) and vs. average detection rate (right).

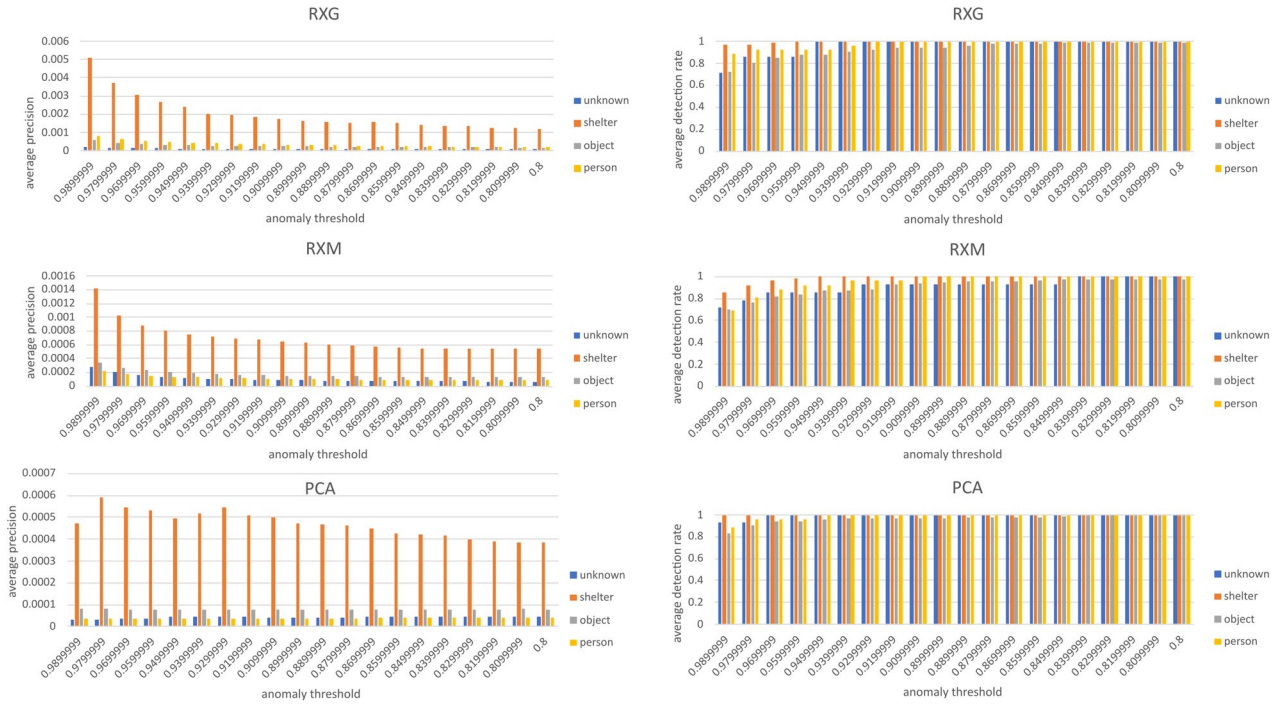

Fig. 7 Performance of model-based color anomaly detectors (RXG,RXM,PCA) over each class (unknown, shelter, object, person). Anomaly threshold vs. average precision (left) and vs. average detection rate (right).

Our experiments reveal that existing color anomaly detectors perform poorly on our dataset –both in comparison to human observers and under occlusion conditions. Deep-learning-based methods achieve precisions of below 3.5% (or just over 10% for individual classes) and detection rates under 30%. Model-based approaches reach near 100% detection rates but suffer from extremely low precision (<0.75%). Unlike our

human volunteers, these methods rely solely on local image regions or individual pixels, lacking broader contextual awareness. Anomalies detected in small regions may lose significance if they appear frequently at a global scale. These results highlight the urgent need for advancements in context-aware anomaly detection to ensure reliable performance in complex forested environments for search missions.

It is important to note that our benchmarking study is designed solely to demonstrate the applicability of our dataset, not to evaluate the performance of individual detectors in depth. In particular, the deep-learning-based detectors could likely achieve better results if fine-tuned specifically for forested terrain.

We also evaluated automated object classification as an alternative to anomaly detection. Using our dataset, we divided the labeled samples into training, validation, and test sets and trained YOLOv12[98], a state-of-the-art classifier commonly employed in search-and-rescue missions, to detect anomalies across our four categories: persons, shelters, objects, and unknown. However, object classification completely failed with extremely low confidence scores in this experiment (0.016% on average with a maximum of 2.6%). The reason for this was already discussed in previous works[82,83]: Occlusion of dense vegetation obscures critical clues – many of which occupied only a few pixels. Under such conditions, even deep neural networks struggled to generalize and automated object classification remains unrealistic.

Usage Notes

Limitations of our dataset include the following: 1). Anomalies are annotated using bounding boxes, as more precise segmentation masks are challenging to obtain due to partial occlusion by vegetation. 2). The findings rely on human volunteers, introducing a degree of subjectivity in labeling. 3). The dataset consists exclusively of aerial images captured under clear skies to maximize light reflections from densely occluded forest floors.

Note that to save new findings to the dataset, a password is required, which can be obtained from the corresponding author.

Data availability

The dataset generated in this study are publicly available. The core labeled benchmark dataset is hosted on Zenodo (https://zenodo.org/records/15848419)[97], while the complete dataset, including additional unlabeled imagery and an interactive annotation interface, is accessible at https://weitefeld.cg.jku.at/. A map-based overview of the entire dataset is provided at https://macs.dlr.de/weitefeld/.

Code availability

The code for our image pre-processing and benchmark study is available at: https://zenodo.org/records/15848419[97].

Received: 14 July 2025; Accepted: 19 March 2026;
Published online: 25 March 2026

References

1. Reed, I. S. & Yu, X. Adaptive multiple-band CFAR detection of an optical pattern with unknown spectral distribution. *IEEE Transactions on Acoustics, Speech, and Signal Processing* **38**, 1760–1770 (1990).
2. Ndiour, I., Ahuja, N. A., Genc, E. U. & Tickoo, O. FRE: A Fast Method For Anomaly Detection And Segmentation. in *Proceedings of the 34th British Machine Vision Conference (BMVC), Aberdeen, UK, November 20-24, 2023* (BMVA, 2023).
3. Yu, J. *et al*. Fastflow: Unsupervised anomaly detection and localization via 2D normalizing flows. *arXiv preprint arXiv:2111.07677* (2021).
4. Batzner, K., Heckler, L. & König, R. EfficientAD: Accurate visual anomaly detection at millisecond-level latencies in *Proceedings of the IEEE/CVF Winter Conference on Applications of Computer Vision*, 128–138 (2024).
5. Chang, C.-I. & Chiang, S.-S. Anomaly detection and classification for hyperspectral imagery. *IEEE Transactions on Geoscience and Remote Sensing* **40**, 1314–1325 (2002).
6. Shyu, M.-L., Chen, S.-C., Sarinnapakorn, K. & Chang, L. A novel anomaly detection scheme based on principal component classifier in *Proceedings of the IEEE Foundations and New Directions of Data Mining Workshop*, 172–179 (2003).
7. Proft, J., Suarez, J. & Murphy, R. Spectral anomaly detection with machine learning for wilderness search and rescue in *2015 IEEE MIT Undergraduate Research Technology Conference*, 1–3 (2015).
8. Morse, B. S., Thornton, D. & Goodrich, M. A. Color anomaly detection and suggestion for wilderness search and rescue in *Proceedings of the Seventh Annual ACM/IEEE International Conference on Human-Robot Interaction*, 455–462 (2012).
9. Marshall, T. & Perkins, L. N. Color outlier detection for search and rescue. *Dept. Elect. Comput. Eng., Boston Univ., Boston, MA, USA, Tech. Rep. ECE-2015-01* (2015).
10. Hoai, D. K. & Van Phuong, N. Anomaly color detection on UAV images for search and rescue works in *2017 9th International Conference on Knowledge and Systems Engineering (KSE)*, 287–291 (2017).
11. Cui, C. & Xu, J. A DWT-SVDD anomaly detection algorithm using hyperspectral remote sensing in marine search and rescue in *2021 IEEE 6th International Conference on Signal and Image Processing (ICSIP)*, 181–184 (2021).
12. Agcayazi, M. T., Cawi, E., Jurgenson, A., Ghassemi, P. & Cook, G. ResQuad: Toward a semi-autonomous wilderness search and rescue unmanned aerial system in *2016 International Conference on Unmanned Aircraft Systems (ICUAS)*, 898–904 (2016).
13. Morandini, L. Anomaly detection from aerial images for search and rescue missions. M.Sc. Thesis, *School of Industrial and Information Engineering, Politecnico di Milano*. Available at: https://hdl.handle.net/10589/206674 (2021)
14. Sime, R. & Loveland, R. Anomaly detection methods for maritime search and rescue in *Proceedings of the 14th International Conference on Pattern Recognition Applications and Methods (ICPRAM)*, 1, 764–770 (SciTePress, 2025). ISBN: 978-989-758-730-6.
15. Seits, F., Kurmi, I. & Bimber, O. Evaluation of color anomaly detection in multispectral images for synthetic aperture sensing. *Eng* **3**, 541–553 (2022).
16. Zavala-Vazquez, F., Correa-Tome, F. E., Hernandez-Belmonte, U. H. & Ramirez-Paredes, J.-P. Anomaly detection in aerial imagery using color and texture features in *2019 International Conference on Mechatronics, Electronics and Automotive Engineering (ICMEAE)*, 45–49 (2019).
17. He, M. & Chen, H. Anomaly detection in species distribution patterns: A spatio-temporal approach for biodiversity conservation. *Journal of Biobased Materials and Bioenergy* **18**, 39–50 (2024).

18. Rippel, O., Haumering, P., Brauers, J. & Merhof, D. Anomaly detection for the automated visual inspection of PET preform closures in *2021 26th IEEE International Conference on Emerging Technologies and Factory Automation (ETFA)*, 1–7 (2021).
19. Hung, Y.-H. Developing an anomaly detection system for automatic defective products' inspection. *Processes* **10**, 1476 (2022).
20. Yuan, M., Muhammad, A., Rukshan, H., Tan, D. & Somani, N. A collaborative robotic approach for inspection and anomaly detection in industrial applications in *Social Robotics: 13th International Conference, ICSR 2021, Singapore, Proceedings 13*, 757–762 (2021).
21. Kähler, F., Schmedemann, O. & Schüppstuhl, T. Anomaly detection for industrial surface inspection: application in maintenance of aircraft components. *Procedia CIRP* **107**, 246–251 (2022).
22. Lai, Y.-T. K., Hu, J.-S., Tsai, Y.-H. & Chiu, W.-Y. Industrial anomaly detection and one-class classification using generative adversarial networks in *2018 IEEE/ASME International Conference on Advanced Intelligent Mechatronics (AIM)*, 1444–1449 (2018).
23. Lehr, J., Sargsyan, A., Pape, M., Philipps, J. & Krüger, J. Automated optical inspection using anomaly detection and unsupervised defect clustering in *2020 25th IEEE International Conference on Emerging Technologies and Factory Automation (ETFA)*, 1, 1235–1238 (2020).
24. Haselmann, M., Gruber, D. P. & Tabatabai, P. Anomaly detection using deep learning based image completion in *2018 17th IEEE International Conference on Machine Learning and Applications (ICMLA)*, 1237–1242 (2018).
25. Tang, T.-W. *et al*. Anomaly detection neural network with dual auto-encoders GAN and its industrial inspection applications. *Sensors* **20**, 3336 (2020).
26. Saeedi, J. & Giusti, A. Anomaly detection for industrial inspection using convolutional autoencoder and deep feature-based one-class classification. in *VISIGRAPP (5: VISAPP)*, 85–96 (2022).
27. Shah, R. A. & Kim, H. Advanced color pseudo anomaly to enhance learning of convolutional neural network models in *2023 IEEE International Conference on Consumer Electronics-Asia (ICCE-Asia)*, 1–3 (2023).
28. Du, Y. *et al*. Anomaly detection in fundus images by self-adaptive decomposition via local and color based sparse coding. *Biomedical Optics Express* **13**, 4261–4277 (2022).
29. Wan, H.-P., Zhu, Y.-K., Luo, Y. & Todd, M. D. Unsupervised deep learning approach for structural anomaly detection using probabilistic features. *Structural Health Monitoring* **24**, 3–33 (2025).
30. Bergmann, P., Batzner, K., Fauser, M., Sattlegger, D. & Steger, C. Beyond dents and scratches: Logical constraints in unsupervised anomaly detection and localization. *International Journal of Computer Vision* **130**, 947–969 (2022).
31. Lile, C. & Yiqun, L. Anomaly detection in thermal images using deep neural networks in *2017 IEEE International Conference on Image Processing (ICIP)*, 2299–2303 (2017).
32. Sledz, A. & Heipke, C. Thermal anomaly detection based on saliency analysis from multimodal imaging sources (2021).
33. Lee, E. K., Viswanathan, H. & Pompili, D. Model-based thermal anomaly detection in cloud datacenters using thermal imaging. *IEEE Transactions on Cloud Computing* **6**, 330–343 (2015).
34. Sledz, A., Unger, J. & Heipke, C. UAV-based thermal anomaly detection for distributed heating networks. *The International Archives of the Photogrammetry, Remote Sensing and Spatial Information Sciences* **43**, 499–505 (2020).
35. Burkard, E., Bulatov, D. & Kottler, B. Towards detection of thermal anomalies in large urban areas using simulation. *The International Archives of the Photogrammetry, Remote Sensing and Spatial Information Sciences* **43**, 1195–1202 (2020).
36. Nikolov, I. A. *et al*. Seasons in drift: A long-term thermal imaging dataset for studying concept drift in *Thirty-fifth Conference on Neural Information Processing Systems* (2021).
37. Tadros, A. *et al*. Anomaly detection for hotspot identification in Landsat images in *IGARSS 2024-2024 IEEE International Geoscience and Remote Sensing Symposium*, 8218–8222 (2024).
38. Vollmer, E., Ruck, J., Volk, R. & Schultmann, F. Detecting district heating leaks in thermal imagery: Comparison of anomaly detection methods. *Automation in Construction* **168**, 105709 (2024).
39. Li, S., Zhang, K., Hao, Q., Duan, P. & Kang, X. Hyperspectral anomaly detection with multiscale attribute and edge-preserving filters. *IEEE Geoscience and Remote Sensing Letters* **15**, 1605–1609 (2018).
40. Jaenisch, H. & Handley, J. Data model LUT-based change and anomaly detection for real-time multispectral image characterization. *Algorithms and Technologies for Multispectral, Hyperspectral, and Ultraspectral Imagery XVIII* **8390**, 323–335 (2012).
41. Leon-Lopez, K. M., Mouret, F., Arguello, H. & Tourneret, J.-Y. Anomaly detection and classification in multispectral time series based on hidden Markov models. *IEEE Transactions on Geoscience and Remote Sensing* **60**, 1–11 (2021).
42. Ziemann, A., Simonoko, H. & Flynn, E. Temporal anomaly detection in multispectral imagery in *IGARSS 2020-2020 IEEE International Geoscience and Remote Sensing Symposium*, 3975–3978 (2020).
43. Su, H., Wu, Z., Zhang, H. & Du, Q. Hyperspectral anomaly detection: A survey. *IEEE Geoscience and Remote Sensing Magazine* **10**, 64–90 (2021).
44. Wang, Z. *et al*. Hyperspectral anomaly detection based on variational background inference and generative adversarial network. *Pattern Recognition* **143**, 109795 (2023).
45. Cheng, B. & Gao, Y. Hyperspectral anomaly detection via low-rank and sparse decomposition with cluster subspace accumulation. *Scientific Reports* **14**, 29530 (2024).
46. Raza Shah, N. *et al*. Hyperspectral anomaly detection: a performance comparison of existing techniques. *International Journal of Digital Earth* **15**, 2078–2125 (2022).
47. Xu, Y., Wu, Z., Li, J., Plaza, A. & Wei, Z. Anomaly detection in hyperspectral images based on low-rank and sparse representation. *IEEE Transactions on Geoscience and Remote Sensing* **54**, 1990–2000 (2015).
48. Lei, J., Xie, W., Yang, J., Li, Y. & Chang, C.-I. Spectral-spatial feature extraction for hyperspectral anomaly detection. *IEEE Transactions on Geoscience and Remote Sensing* **57**, 8131–8143 (2019).
49. Liu, J. *et al*. Deep industrial image anomaly detection: A survey. *Machine Intelligence Research* **21**, 104–135 (2024).
50. Hu, X. *et al*. Hyperspectral anomaly detection using deep learning: A review. *Remote Sensing* **14**, 1973 (2022).
51. Singh, P. & Pankajakshan, V. A deep learning based technique for anomaly detection in surveillance videos in *2018 Twenty Fourth National Conference on Communications (NCC)*, 1–6 (2018).
52. Munir, M., Siddiqui, S. A., Dengel, A. & Ahmed, S. DeepAnT: A deep learning approach for unsupervised anomaly detection in time series. *IEEE Access* **7**, 1991–2005 (2018).
53. Wang, R., Nie, K., Wang, T., Yang, Y. & Long, B. Deep learning for anomaly detection in *Proceedings of the 13th International Conference on Web Search and Data Mining*, 894–896 (2020).
54. Simon, D. L. & Rinehart, A. W. A model-based anomaly detection approach for analyzing streaming aircraft engine measurement data. *American Society of Mechanical Engineers* (2014).
55. Gatfaoui, I., Solaiman, B. & Farah, I. R. Model based anomaly detection in high dimensional DATA in *2022 6th International Conference on Advanced Technologies for Signal and Image Processing (ATSIP)*, 1–6 (2022).
56. Mehrotra, K. G., Mohan, C. K. & Huang, H. in *Anomaly Detection Principles and Algorithms*, 57–94, https://doi.org/10.1007/978-3-319-67526-8_5 (Springer International Publishing, Cham, 2017). ISBN: 978-3-319-67526-8.
57. Xia, X. *et al*. GAN-based anomaly detection: A review. *Neurocomputing* **493**, 497–535 (2022).
58. Bergmann, P., Fauser, M., Sattlegger, D. & Steger, C. MVTec AD-A comprehensive real-world dataset for unsupervised anomaly detection in *Proceedings of the IEEE/CVF Conference on Computer Vision and Pattern Recognition*, 9592–9600 (2019).
59. Bergmann, P., Batzner, K., Fauser, M., Sattlegger, D. & Steger, C. The MVTec anomaly detection dataset: A comprehensive real-world dataset for unsupervised anomaly detection. *International Journal of Computer Vision* **129**, 1038–1059 (2021).

60. Heckler-Kram, L., Neudeck, J.-H., Scheler, U., König, R. & Steger, C. The MVTec AD 2 dataset: Advanced scenarios for unsupervised anomaly detection. *International Journal of Computer Vision* **134**, 175 (2026).
61. Bergmann, P., Jin, X., Sattlegger, D. & Steger, C. The MVTec 3D-AD dataset for unsupervised 3D anomaly detection and localization in *Proceedings of the 17th International Joint Conference on Computer Vision, Imaging and Computer Graphics Theory and Applications – VISAPP*, 202–213 (SciTePress, 2022).
62. Mishra, P., Verk, R., Fornasier, D., Piciarelli, C. & Foresti, G. L. VT-ADL: A vision transformer network for image anomaly detection and localization in *2021 IEEE 30th International Symposium on Industrial Electronics (ISIE)*, 01–06 (2021).
63. Wang, S. & Miao, Z. Anomaly detection in crowd scene in *IEEE 10th International Conference on Signal Processing Proceedings*, 1220–1223 (2010).
64. Lu, C., Shi, J. & Jia, J. Abnormal event detection at 150 fps in MATLAB in *Proceedings of the IEEE International Conference on Computer Vision*, 2720–2727 (2013).
65. Pranav, M. *et al*. A day on campus-an anomaly detection dataset for events in a single camera in *Proceedings of the Asian Conference on Computer Vision* (2020).
66. Liu, W., Luo, W., Lian, D. & Gao, S. Future frame prediction for anomaly detection-a new baseline in *Proceedings of the IEEE Conference on Computer Vision and Pattern Recognition*, 6536–6545 (2018).
67. Jin, P., Mou, L., Xia, G.-S. & Zhu, X. X. Anomaly detection in aerial videos with transformers. *IEEE Transactions on Geoscience and Remote Sensing* **60**, 1–13 (2022).
68. Verma, U. *et al*. Contextual information based anomaly detection for multi-scene aerial videos. *Scientific Reports* **15**, 1–18 (2025).
69. Tran, T. M., Vu, T. N., Nguyen, T. V. & Nguyen, K. UIT-ADrone: A novel drone dataset for traffic anomaly detection. *IEEE Journal of Selected Topics in Applied Earth Observations and Remote Sensing* **16**, 5590–5601 (2023).
70. Madan, N. *et al*. Self-supervised masked convolutional transformer block for anomaly detection. *IEEE Transactions on Pattern Analysis and Machine Intelligence* **46**, 525–542 (2023).
71. Chan, R. *et al*. SegmentMeIfYouCan: A benchmark for anomaly segmentation. in *Proceedings of the Neural Information Processing Systems Track on Datasets and Benchmarks (NeurIPS)* (2021).
72. Singh, H., Hand, E. M. & Alexis, K. Anomalous motion detection on highway using deep learning in *2020 IEEE International Conference on Image Processing (ICIP)*, 1901–1905 (2020).
73. Blum, H., Sarlin, P.-E., Nieto, J., Siegwart, R. & Cadena, C. Fishyscapes: A benchmark for safe semantic segmentation in autonomous driving in *Proceedings of the IEEE/CVF International Conference on Computer Vision Workshops*, 0–0 (2019).
74. Pinggera, P. *et al*. Lost and found: Detecting small road hazards for self-driving vehicles in *2016 IEEE/RSJ International Conference on Intelligent Robots and Systems (IROS)*, 1099–1106 (2016).
75. Zou, Y., Jeong, J., Pemula, L., Zhang, D. & Dabeer, O. Spot-the-difference self-supervised pre-training for anomaly detection and segmentation in *European Conference on Computer Vision*, 392–408 (2022).
76. Ramachandra, B. & Jones, M. Street scene: A new dataset and evaluation protocol for video anomaly detection in *Proceedings of the IEEE/CVF Winter Conference on Applications of Computer Vision*, 2569–2578 (2020).
77. Jia, S. & Qian, Y. Spectral and spatial complexity-based hyperspectral unmixing. *IEEE Transactions on Geoscience and Remote Sensing* **45**, 3867–3879 (2007).
78. Zhao, R., Du, B. & Zhang, L. A robust nonlinear hyperspectral anomaly detection approach. *IEEE Journal of Selected Topics in Applied Earth Observations and Remote Sensing* **7**, 1227–1234 (2014).
79. Gillis, D., Bowles, J. H. & Winter, M. E. Using endmembers as a coordinate system in hyperspectral imagery. *Imaging Spectrometry VIII* **4816**, 346–354 (2002).
80. Gader, P., Zare, A., Close, R., Aitken, J. & Tuell, G. MUUFL Gulfport hyperspectral and LiDAR airborne data set. Univ. Florida, Gainesville, FL, USA, Tech. Rep. REP-2013-570 (2013).
81. Acito, N., Matteoli, S., Rossi, A., Diani, M. & Corsini, G. Hyperspectral airborne "Viareggio 2013 Trial" data collection for detection algorithm assessment. *IEEE Journal of Selected Topics in Applied Earth Observations and Remote Sensing* **9**, 2365–2376 (2016).
82. Schedl, D. C., Kurmi, I. & Bimber, O. Search and rescue with airborne optical sectioning. *Nature Machine Intelligence* **2**, 783–790 (2020).
83. Schedl, D. C., Kurmi, I. & Bimber, O. An autonomous drone for search and rescue in forests using airborne optical sectioning. *Science Robotics* **6**, eabg1188 (2021).
84. Song, Z. *et al*. An infrared dataset for partially occluded person detection in complex environment for search and rescue. *Scientific Data* **12**, 300 (2025).
85. Bondi, E. *et al*. BIRDSAI: A dataset for detection and tracking in aerial thermal infrared videos in *Proceedings of the IEEE/CVF Winter Conference on Applications of Computer Vision*, 1747–1756 (2020).
86. Thoreau, M. & Wilson, F. SaRNet: A dataset for deep learning assisted search and rescue with satellite imagery in *2021 12th International Symposium on Image and Signal Processing and Analysis (ISPA)*, 204–208 (2021).
87. Sambolek, S. & Ivasic-Kos, M. Automatic person detection in search and rescue operations using deep CNN detectors. *IEEE Access* **9**, 37905–37922 (2021).
88. Božić-Štulić, D., Marušić, Ž. & Gotovac, S. Deep learning approach in aerial imagery for supporting land search and rescue missions. *International Journal of Computer Vision* **127**, 1256–1278 (2019).
89. Broyles, D., Hayner, C. R. & Leung, K. Wisard: A labeled visual and thermal image dataset for wilderness search and rescue in *2022 IEEE/RSJ International Conference on Intelligent Robots and Systems (IROS)*, 9467–9474 (2022).
90. Bernal, A. M. R., Scheirer, W. & Cleland-Huang, J. NOMAD: A Natural, Occluded, Multi-scale Aerial Dataset, for Emergency Response Scenarios in *2024 IEEE/CVF Winter Conference on Applications of Computer Vision (WACV)*, 8569–8580 (2024).
91. Zhang, X., Feng, Y., Wang, N., Lu, G. & Mei, S. Aerial Person Detection for Search and Rescue: Survey and Benchmarks. *Journal of Remote Sensing*, 0474 (2025).
92. Zhang, Y. *et al*. Drone-based RGBT tiny person detection. *ISPRS Journal of Photogrammetry and Remote Sensing* **204**, 61–76 (2023).
93. Akshatha, K. *et al*. Manipal-UAV person detection dataset: A step towards benchmarking dataset and algorithms for small object detection. *ISPRS Journal of Photogrammetry and Remote Sensing* **195**, 77–89 (2023).
94. Brogan, J. *et al*. Expanding Accurate Person Recognition to New Altitudes and Ranges: The BRIAR Dataset tech. rep. (Oak Ridge National Laboratory (ORNL), Oak Ridge, TN, United States, 2022).
95. Brauchle, J. *et al*. Capabilities and Applications of MACS Aerial Camera Systems for Environmental Research in *EGU General Assembly 2021* https://elib.dlr.de/142914/ (2021).
96. Forsey, A. & Gungor, S. Demosaicing images from colour cameras for digital image correlation. *Optics and Lasers in Engineering* **86**, 20–28 (2016).
97. Nathan, A. A. R. J. *et al*. An aerial color image anomaly dataset for search missions in complex forested terrain https://doi.org/10.5281/zenodo.15848419 (Zenodo, 2025).
98. Tian, Y., Ye, Q. & Doermann, D. YOLOv12: Attention-Centric Real-Time Object Detectors. *arXiv preprint arXiv:2502.12524* (2025).

Acknowledgements

We extend our sincere gratitude to all 160 volunteers who supported this mission by participating in the online crowd sourcing. A special thanks goes to the operational command of the Rhineland-Palatinate police for their outstanding cooperation, as well as to the over 1,000 police officers in the field for their dedicated efforts.

Author contributions

M.B., M.G., and O.B. collected the data. R.J.A.A.N., M.G., M.M., N.Ö., M.Y., B.P., and O.B. processed the data. N.Ö. implemented the web interface and annotated bounding box labels. R.J.A.A.N. carried out the benchmarking study. O.B. designed, organized, carried out, and supervised the online crowd sourcing and reviewed the data. M.M. implemented the mapping of the data. M.G. implemented the backprojection of labels. O.B., R.J.A.A.N., N.Ö., and M.G. wrote the paper. O.B., M.G., and R.B. supervised the work and managed the project. All authors reviewed the manuscript.

Competing interests

The authors declare no competing interests.

Additional information

Correspondence and requests for materials should be addressed to O.B.

Reprints and permissions information is available at www.nature.com/reprints.

Publisher's note Springer Nature remains neutral with regard to jurisdictional claims in published maps and institutional affiliations.